Fluid migrations and volcanic earthquakes from depolarized ambient noise

Simona Petrosino
Istituto Nazionale di Geofisica e Vulcanologia - Osservatorio Vesuviano
Luca De Siena (ldesiena@uni-mainz.de)
Institute of Geosciences, Johannes Gutenberg University

Article

Keywords: ambient noise, volcano, volcanic earthquakes

Posted Date: May 21st, 2021

DOI: https://doi.org/10.21203/rs.3.rs-470597/v1

Version of Record: A version of this preprint was published at Nature Communications on November 17th, 2021. See the published version at https://doi.org/10.1038/s41467-021-26954-w.

Abstract

Ambient noise polarizes inside low-velocity fault zones, yet the spatial and temporal resolution of polarized noise on gas-bearing fluids migrating through stressed volcanic systems is unknown. Pressurized fluids increase stress and lead to volcanic earthquakes; imaging their location in real time would be a giant leap toward forecasting eruptions and monitoring volcanic unrest. Here, we show that depolarized noise detects fluid injections and migrations leading to earthquakes inside the laterally-stressed hydrothermal systems of Campi Flegrei caldera (Southern Italy). A polarized transfer structure connects the deforming centre of the caldera to open hydrothermal vents and extensional caldera-bounding faults during periods of low seismic release. Fluids depolarize the transfer structure and pressurize the hydrothermal system, building up stress before earthquakes and migrating after seismic sequences. During sequences, fluid migration pathways connect the location of the last eruption (Monte Nuovo, 1538AD) with the part of the eastern caldera trapped between transfer and extensional structures. After recent intense seismicity (December 2019-April 2020), the transfer structure appears sealed while fluids stored in the east caldera have moved further east. Depolarized noise has the potential to monitor fluid migrations and earthquakes at stressed volcanoes quasi-instantaneously and with minimum processing.

Main

We have learned how to use noise produced by humans, ocean swell, and atmosphere solid-Earth interactions[12,13] to illuminate the interior of magmatic and hydrothermal systems[14-17]. Noise data from expanding seismic networks are analyzed with novel array[20] and interferometric[21,22] techniques, allowing detection of volcanic processes and forecasting hazards without having to wait for earthquakes[18,19]. *Noise polarization* across dip-angle normal faults has been related to stress and variations in stiffness anisotropy[1,2]. However, the potential of noise polarization to illuminate pressurized fluids in volcanic systems is yet to be explored. Campi Flegrei (Southern Italy, Fig. 1a, small lower panel) is an inhabited volcanic caldera bordering Naples (the third most populous city of Italy) and the ideal location to discover this potential. The caldera is a capped[11,23-26] geothermal system, where hazardous CO_2-bearing fluids propagate from the primary deformation source (Figs. 1-3, black dot) to fumaroles (S) at least since 1984[5-11,23-26]. Heating of the hydrothermal system, volcanic gas emissions at the surface[5-8] and seismic release[5,7,8,27,28] result from consecutive episodes of unrest, promoting a long-term accumulation of lateral stress and expanding reservoirs[4,5]. Accumulated stress and fluid migrations left marks across extensional faults and feeding systems at the caldera. Polarized noise can see through the overlying rocks to catch these marks. The azimuth of the horizontal polarization vector derived from ambient noise and the resultant length of its distribution (R)[1,2,29,30] are used here for the first time as both imaging and diagnostic tools (Methods, 0.2-1 Hz). During periods of low seismic release[31,32], they detect the hypothesized link between deep extensional and caldera-bounding faults (*extensional structures*) that bear regional stress[33-37] north and east of the caldera (Fig. 1a, white dotted line), and a dynamic *transfer*

structure[34] that crosses its deforming centre and vents outgassing at the surface[6-10] (Fig. 1a, black dotted line). At higher frequencies (1-5 Hz, Methods, Extended Data Fig. 1), regional and caldera-bounding faults disappear due to the sensitivity of noise to shallower and smaller structures[13,29]. High resultant lengths and polarized azimuths mark NW-SE-trending extensional faults[34-37] with exceptional stability between 2009 and 2020 (Figs. 1, Methods, Extended Data Figs. 1-5). The transfer structure develops instead SW-NE (Fig. 1a), the direction of the volcanic ridge under the caldera[34]. When hydrothermal pressure, gas emission and seismicity increase (2018)[31,32], the transfer structure depolarizes, allowing to monitor fluid migrations leading to high-duration-magnitude (Md>3) earthquakes (Figs. 1b-d).

The polarized extensional and transfer structures are a direct consequence of processes that have been consistently imaged and monitored during the last thirty-six years. The high-attenuation[24] signature of the repeated injections[25] that caused the strongest volcano-tectonic event recorded at the caldera (Md=4.1) appears as an unpolarized anomaly after more than three decades (Fig. 2a). The central hydrothermal system opened in the WSW-ENE direction on April 1st, 1984 (black diamonds, Fig. 2a) due to a NW-directed injection of magma[9], magmatic or supercritical fluids[23-25]. After thirty years (2011-13), a low-velocity aseismic reservoir[17,38] had expanded from the injection point (Fig. 2b, black cross). Expansion toward west and north continued until fluids had reached the western caldera-bounding faults, producing high magnitude earthquakes in 2012[4,5,17] (Fig 2b, western black diamonds). However, no apparent lateral expansion was visible east and south of the injection point (black cross, Fig. 2a,b). Fluids stopped at a barrier delineated by high velocities and high stresses, as shown by combined seismic and InSAR interferometric analyses[10]. This barrier coincides with the transfer structure that crosses the eastern sector of the Solfatara crater (Fig. 2b). Here, shear-wave-splitting anisotropy[39], InSAR[11], and gravity gradiometry[33] identify a SN anomaly that accumulates the highest lateral stress during unrest[10], producing small-magnitude earthquakes[31] (Fig 2b, diamonds).

Imaging stressed fluid-filled structures

In the eastern caldera, the highest resultant lengths show azimuths consistently parallel to the NW-SE high-velocity extensional faults[11,35-37] (Fig. 1). The area is wide enough to become a high-velocity waveguide for horizontally-polarized isotropic S waves generated either in the centre of the Tyrrhenian Sea[12] or across the near coastline (Extended Data Fig. 7a,b). This waveguide explains azimuths parallel to the trend for both source configurations at stations with $R>0.25$ (Methods). Still, a far-field source[12] better fits azimuths observed across the entire caldera (Extended Data Fig. 7a,b, Residuals). Far-field sources cannot explain azimuths perpendicular to the primary direction (SW-NE) of the transfer structure between 2009 and 2017 (Fig. 1a). These azimuths could be a consequence of seismic anisotropy, which tracks permanent directional signatures from the deep Earth mantle[40] to hydrated subducting slabs[41]. If low-velocity faults are wide enough, stiffness anisotropy[1,2] and trapping and reverberations[42] on high-dip fault walls can polarize noise perpendicular to fault walls. Across the transfer structure, azimuths indeed develop perpendicular to high-dip fault walls (Fig. 2c) and crack anisotropy at least at Solfatara[39]. Yet,

the transfer structure is a small *high-velocity structure* (Fig. 2b)[17] consequence of lateral stress accumulated in the crust[4,5,10]. Azimuths across this structure better fit those obtained for sources generated at the near coastline[12] (Extended Data Fig. 7a,b right). Near-field sources[7] seem a more likely controller of azimuths than anisotropy, yet anisotropy increases polarization across similarly compressed structures[21,22].

Depolarization of the 2009-2017 transfer structure is central to explain stress release and structural changes in the volcano. While the extensional trend appears consistent over time, the transfer structure only polarizes during periods of lower seismic and geochemical release[31,32], when deep injections and hydrothermal recharge are sparse and rarely coupled[6-8,27,31,32] (Fig. 1a). The structure is in contact with the high-attenuation[24] and deforming[9,10] location of deep injections (Fig. 2a, black cross). It runs along:

1. the semi-circular east and north borders of a reservoir that was expanding in 2011-2013[17] (Fig. 2b);
2. the lobe-shaped maxima of horizontal stresses observed using InSAR methods[10];
3. an abrupt structural variation in tidal tilting from WE to SW-NE[43,44].

The dynamics associated with these geophysical responses and maps are linked to the sub-caprock migration of over-saturated CO_2-bearing fluids[5-11,17,19,23], adding persistent low-frequency noise and long-period events[30]. The high-scattering fluids rising and migrating from deep injections pervade fractures, producing local noise that progressively intensifies[7] and depolarizes the transfer structure (Fig. 1b,c). In the presence of high-velocity contrasts, stations within one wavelength from such extended sources lose polarization in the heterogeneous medium (Extended Data Fig. 7a,b, right, *R* decrease at station ACL2). This behaviour is apparent at Solfatara in 2018, when the central and eastern unpolarized reservoirs connect (Figs. 1b). Fluids eventually outflow on metasediments[11] between transfer and extensional structures. These high-attenuation[24,25] sediments reduce ambient noise directionality between 0.2 and 1 Hz[45] and are the most consistent unpolarized anomaly during the decade (Fig. 1).

The pre-seismic (Fig. 1c) and post-seismic (Fig. 1d) patterns show the progressive depolarization induced by fluids migrating from the injection location to: (1) the eastern sector of Solfatara and the Pisciarelli vent (S, Fig. 1), where the geochemical unrests of the last fifteen years have been monitored[6,11]; (2) Monte Nuovo, the location of the last eruption at Campi Flegrei (M, 1538AD). The Solfatara-Pisciarelli vents emit from 2000 to 3000 tons/day of CO_2 in the atmosphere[7,8]. They have been consistently deforming toward the east in the last 20 years[46], moving along with seismicity from the injection location[25,38]. Joint interpretations of resistivity, geochemistry and field data[11,36] detect the plume that feeds these vents, the surrounding metasediments, and the eastern extensional faults that bind low-density metasomatized rocks[11] (Fig. 2c). In the western portion of Fig. 2c, the transfer structure crosses the capped resistive plume that stores steam and gas, feeding fumaroles. Here, injections of fluids from depth[6-11,23-26,47] coupled with meteoric recharge[27,28,43] produce stress[10] and outflow eastern liquid-bearing sediments[11]. Gas-bearing fluids over-pressurized the eastern caldera between 2011 and 2013[19]

due to concurrent lateral expansion[10] of the source region and saturation of the reservoirs[6-8]. The depolarization of the transfer structure that started in 2018 (Fig. 1b) led to the highest seismic release in thirty-six years at the caldera[31,32]. The area east of the Solfatara feeder was already suffering the highest horizontal stress in 2011-13 (white diamond[10], Fig. 2b,c). Here, fluid injections from depth coupled with progressive permeability increases from heavy rains[27,28,43] started the seismic sequence in December 2019[31]. Stresses on the high-dip fault east of Solfatara (Figs. 2c and 3) generated two high-magnitude volcano-tectonic events[7,31] after minor earthquake swarms[47]: a Md3.1 on December 6th, 2019 and a Md3.3 on April 26th, 2020 (white circles **1** and **2**, Figs. 1c,d, 2c and 3a,b).

Monitoring stress and fluid migrations

This seismic sequence is the effect of pressurization of the hydrothermal system[32] induced by lateral stress and fluid migrations, which horizontal noise polarization can monitor. The mechanical weakening of the crust[15] and the corresponding depolarization of ambient noise[22] after the Tohoku earthquake detect the release of stress and upward fluid migration at volcanoes hundreds of kilometres afar. In a stressed geothermal environment[23-26] like Campi Flegrei, these surges appear at sharp lateral discontinuities, as caldera-bounding faults. In September 2012, fluid injections activated western caldera faults near Monte Nuovo (Fig. 2b, M, western black diamonds)[9,10]. The resultant lengths measured over months at the nearest station detect the permanent depolarization following the earthquakes, in analogy to interferometric analyses[21,22] (Methods, Extended Data Fig. 8). Fluid migrations between western and eastern caldera were the mechanism that released stress at the end of the 1984 unrest[25]. Months after the 2012 swarm, it is the part of the eastern caldera compressed between transfer and extensional structures (Fig. 1a) that suffered the highest long-lasting velocity reductions (>0.1%)[19]. These reductions are symptomatic of the area bearing the highest concentration of pressurized fluids[15,19], most likely to erupt, form new hydrothermal vents, and nucleate earthquakes[48,49]. The temporal patterns (Figs. 1a-d, 3a,b, Extended Data Figs. 5, 6) clarify that fluid migrations connecting western and eastern caldera coexist and possibly drive stress build-up and release through the seismic sequence. Fluids migrate under the Campi Flegrei caprock[23-25], which forbids surges directly above the primary source of deformation[23]. After each earthquake in 2019-20 (Extended Data Fig. 9), the change in polarization is similar to that observed after the earthquakes in 2012 (Extended Data Fig. 8). It is analogue to the decrease in ambient noise polarization caused by hydrothermal fluid surges at Mount Fuji after the Tohoku earthquake[22]. Unlike Mount Fuji, horizontal stress was already in a critical state at Campi Flegrei due to magma degassing[5-8] and supercritical fluids, pressurized under the caprock[11,23].

During the pre-seismic period (Fig. 1c, 3a), after minor swarms stroke the eastern caldera[7,41], the unpolarized anomaly under the Solfatara and Pisciarelli vents develops from north to south. After the Md3.1 earthquake, this anomaly expanded toward the eastern flank of the Solfatara and the Pisciarelli vents (Fig. 3b), matching the hypothesized low-gravity fluid-ascension path between the two vents[33,36]. During the inter-seismic period, the anomalies in the western and eastern caldera connected across the

seismic pathways that released stress and closed the 1984 unrest[25] (Fig. 3a, diamonds). These maps track fluids generated by the deformation source[6-8] and over-pressurized in the capped system[12,23-26]. The fluids migrated both seismically[31,32] and aseismically in 2020, pressurizing the eastern hydrothermal system until the Md3.3 released stress[7]. The Md3.3 sealed migration by polarizing noise across the transfer structure (Fig. 3a, rightmost panel). By May-June 2020, the eastern unpolarized anomaly was one km east of its original location. It comprised the earthquake location (compare Fig. 3a, left to right) and an area that was polarized before the sequence (Fig. 1a-c). This dislocation is the seismic signature of the persistent lateral stress leading to fluid migrations toward the eastern caldera[38].

Toward monitoring with depolarized noise

Heat increase and critical degassing pressure from depth[6] coupled with hydrothermal recharge[27,28,30,32,43] make the area between regional extension and transfer structure (Fig. 1a,d) most likely to break in the future[48,49]. Once informed by thermo-hydro-mechanical simulations[41], polarization parameters show a quasi-real-time monitoring potential. Recent thermo-hydro-mechanical modelling[47] shows that fluids are injected at the base of faults in the east caldera between three and five days before the Md3.1, depending on injection volumes. Fig 3b and Extended Data Fig. 6 show polarization parameters measured using three hours of noise each day in these periods. After a consistent depolarization five days before the earthquake (Extended Data Fig. 6, 01/12/2019), the *R* increases at all the stations around the location of the Md3.1 (Fig. 3b, pre-seismic), in a manner that is consistent with an increase in compression preceding earthquakes[47]. After the Md3.1, the unpolarized anomaly east of Solfatara expands toward the east (Fig. 3b) with significant statistical variations at stations in the eastern caldera (Extended Data Fig. 9). Similar maps are obtained in a shorter time interval (one to three days) around the Md3.3 to account for the increase in pore pressure following the inter-seismic period[47] (Fig. 3b, Extended Data Fig. 6). Two days before the Md3.3, the eastern unpolarized anomaly had focused on the earthquake location. Two days after the Md3.3, fluids had outflown the area east of the Md3.3[11], depolarizing the eastern extensional trend like after the Md3.1 (Fig. 3b, from left to right). These spatial and temporal relations confirm that depolarized noise can monitor deep sub-caprock[23-27] migrations of fluids preceding and following higher-magnitude earthquakes.

Ambient noise polarization answers the long-standing question of how this stressed volcano feeds its hydrothermal vents and builds and releases stress. A transfer structure connects the central deforming caldera to regional extensional faults[33,34], running under a caprock whose characteristics allow over-pressurization, lateral fluid migration and strong lateral deformation[23]. The area of major volcanic and seismic hazard[48,49] is compressed between transfer and extensional systems. The opening of the transfer structure detects deep fluid migrations toward the surface. These fluids trigger changes in polarization patterns[30], allowing mapping of stress build-up and release through further eastern fluid migrations. Temporal scanning of depolarized noise represents a substantial step toward instantaneous imaging of hydrothermal expansion, leading to earthquakes in stressed calderas. Polarization

measurements from ambient noise interferometry[21,22] require yearly recordings for stable imaging, several days of monitoring measurements, and high amounts of processing. As previously hypothesized[1,2], horizontal noise polarization can achieve similar results using hours of noise and minimal processing.

Methods

Data processing and estimates of horizontal polarization values

The seismic noise recordings used in this study are obtained across eleven years from broadband stations[7,17,19,27] (Fig. 1a). They comprise:

1. Data for the first six months of 2017 obtained from 17 mobile and 6 permanent broadband stations of the INGV – Osservatorio Vesuviano seismic network. The signal was extracted from the continuous six-month-long (January-June) recordings by choosing one week/month and 1hr/day (00:00-01:00 GMT) of each week: an amount of about 42 hours of seismic noise per station. Samples of noise recorded during night-time were chosen to minimize spurious sources caused by anthropic activity[13].
2. Data recorded in 2009 by 20 temporary stations installed during the Unrest seismic campaign[30], and by 4 additional broadband stations (3 mobile and 1 permanent installation) that were in operation in 2009 but no longer in 2017. In this case, due to the short period of acquisition (the Unrest campaign lasted from 9 to 26 March), we extracted samples of three hours (00:00-03:00 GMT) from the continuous recordings performed during the experiment obtaining (on average) about 45 hours of signal/station. The 2009-2017 data set comprises a total of 47 sites (Fig. 1a,b).
3. Data randomly sampled in the first six months of 2018 (recorded between 00:00-03:00 GMT) at 23 broadband stations of the mobile and permanent networks of the INGV – Osservatorio Vesuviano. We extracted about 48 hours of seismic noise per station. In addition, we use 1 hour (of this dataset) at all stations to demonstrate the hourly stability of the patterns across the extensional trend (Fig. 1b-d, Extended Data Fig. 4).
4. Data recorded in 2019 (September-December) and 2020 (January-June) at a higher sampling level to test the monitoring potential before and after earthquakes (Figs. 3-4). The samples were extracted after selecting 9 days/month, except in December 2019 and April 2020. During these months, we selected 12 days in order to sample periods immediately before and after the earthquakes. For each fay we always select the same 3hr (01:00-04:00 GMT). We obtained 117 hr (for 2019) and 171 hr (for 2020) of signal/station at 20 broadband stations of the mobile and permanent network of the INGV – Osservatorio Vesuviano seismic network.

The seismic noise samples were filtered by applying an a-causal Butterworth filter in the bands 0.2-1 Hz and 1–5 Hz. Resultant lengths (R) and azimuths of the seismic wavefield were obtained by applying the covariance matrix method[1,2,29] to three-component seismograms at each station, using contiguous

sliding windows containing three wave cycles of the maximum period. *R* ranges in the interval [0,1]. The closer it is to one, the more concentrated the values around the mean polarization direction are. Data for which the rectilinearity[1,2] was less than 0.5 were discarded, as the angular parameters are associated with seismic wave propagation only if above this threshold[30]. We focused on horizontal ground motion polarization as it is strongly controlled by the medium properties (e.g., presence of faults and cracks)[1,2]. We thus selected the azimuth values associated with a high horizontal polarization degree, fixing an incidence angle < 45° as threshold[1]. Extended Data Figure 1a,b shows *R* and azimuths measured at each station for 2009 and 2017. Panels c and d show the corresponding interpolated mapping. Compared to 0.2-1 Hz, the 1-5 Hz patterns (Extended Data Figure 1b,d) are more affected by anthropic noise[13]. They identify a high-polarization SN structure compatible with a connection between Solfatara and the crater north of it, part of the low-frequency extensional trend. A second high-polarization region characterizes the area north of Monte Nuovo (M, panel d).

Stability of the polarization values between 2009 and 2017.

We compared the results evaluated at five stations (ASBG, CELG, CMSA, CSOB, OMN2 OVDG) of the permanent and mobile networks that were operative in 2009 and 2017. In none of these cases, variations of the polarization features were observed (Extended Data Fig. 2a). A bootstrap test calculated 1000 means of random samples drawn from the R distribution. The subtraction of the average *R* of the real distribution and the bootstrap mean (Extended Data Fig. 2b) shows that, over 47 stations recording in these periods, 41 present minimal changes in *R* (<0.1).

Stability of the polarization patterns measured during 2017 and 2018.

We assess the stability of our results when using data recorded over six months for 2017 and 2018 (Extended Data Fig. 3, blue and orange lines, respectively). A total of 22 stations recorded noise in both periods. The parameters are compared with one hour of signal recorded simultaneously at all stations in 2018 (Extended Data Fig. 3, green, this was possible only for 20 stations). In the figure, there is a 180° periodicity so that apparent changes in azimuths like that at station RENG are uninfluential. Azimuths show minimal differences for *R>0.3* and always within uncertainties, while *R* values are most stable across the extensional trend (red labelled, Extended Data Fig. 3). The comparison between patterns computed over 6 months and 1 hr in 2018 is reported in Extended Data Fig. 4. When considering a single hour, minimal variations are observed across extensional trend.

Monthly and daily variations during seismic unrest

Extended Data Fig. 5 shows the monthly variation in the polarization patterns between September 2019 and June 2020. Monthly variations of *R* and azimuths mean values for the pre- seismic period, during swarms (September-November 2019) show a progressive increase of *R* at all stations. After the Md3.1 earthquake (circled number **1**, December 2019- January 2020) the eastern unpolarized anomaly moves to comprise the earthquake location, while the western caldera polarizes. In the inter-seismic period (January-March 2019) western and eastern unpolarized anomalies connect north of the deformation

source while the eastern unpolarized anomaly moves back to its original location. The Md3.3 post-seismic maps (circled number **2**, May-June 2020) show polarization increases in the sealed central migration system (June 2020), while the eastern unpolarized anomaly moves to the earthquake location. Extended Data Fig. 6 shows the daily variations, where the intervals have been interpreted using the results of thermo-hydro-mechanical modelling[47].

Simulation of isotropic homogeneous horizontal noise polarization

We model noise polarization from an extended line of noise sources located in the central Tyrrhenian basin and from a circle representing noise sources offshore[12]. As sources, we use Morlet wavelets of dominant frequency 0.7 Hz, repeating every 8 s in an isotropic simulation of the wave-equation. The staggered stress-displacement description of SH propagation incorporates viscoelasticity[25] by using memory variables assuming constant-Q Zener model[50]. To obtain seismic velocities from displacements, we apply a finite-impulse-differentiator filter of order 24. The propagation grid extends to the area shown in Fig. 1a (Extended Data Table 1). The strains are obtained from their relationship with displacements, using a spatial derivative operator of fourth order. The discretization of the memory-variable equations is performed using the central differences operator for the time derivative and the mean value operator for the memory variable. Two sponges attenuate boundary propagation.

The finite-difference simulations are most unstable if polarization azimuths are either 0° or 90°[50] and near the center of the caldera for circular polarization. We used grid spacings of 40 m for the two source settings, obtaining *R* varying in the intervals shown in Extended Data Fig. 7a,b. Thus, the simulation grid comprises 750 nodes regularly spaced at 40 m; of these, 150 nodes on each side are allocated for the absorption boundary conditions. The lowest/highest velocities[17] used are 0.5 km/s and 1.5 km/s. For S waves of velocity v_S and a grid step *Dl*, stability is given at times of at least

$$\Delta t = \frac{6}{7\sqrt{3}}\frac{\Delta l}{v_S} = \frac{6}{7\sqrt{3}}\frac{40}{1.5\times10^3} = 12ms$$

in an isotropic medium[49]. To take into account the variations induced by anelasticity and grid dispersion we reduced the time step to *Dt=1* ms. We modelled noise signals lasting 100 s.

We simulated seismograms at all stations recording noise in 2009-2017 and having a minimum *R*=0.25 in the results (Extended Data Fig. 7a,b). The decrease in the homogeneous cases (Extended Data Fig. 7a) is due to numerical instability and boundary conditions. It is lowest in the far field case (Extended Data Fig. 7a) but remains below 1% at all stations for both source configurations. The polarization parameters are retrieved with a blind test. L.D.S. ran simulations while S.P. processed synthetic seismograms without inputs on the original source polarization. The results for the homogeneous cases are shown in Fig. 7a and are compared with real azimuths in Fig. 7c. The square residuals between azimuths in the two source configurations indicate that a far field source is on average more likely to reproduce results (a line residual of 208 against 294).

Simulation of isotropic heterogeneous horizontal noise polarization

The results of the polarization analysis (Fig. 1a) are inserted in the propagation matrix with a 50% increase in shear modulus, a value derived by ambient noise tomography[17] and fixing constant density values[4]. The change is applied only to nodes where *R>0.31* (Extended Data Fig. 7b). For the extensional path, we restricted the area of change to within the extensional faults. The results of the blind tests show a strong reduction of *R* at station ACL2 (*R*~0.5), the only station both inside the waveguide and within one wavelength from noise sources. Without waveguide and with the same source configuration, no near-field trapped wave responsible for decreasing polarization can develop. This explains lower *R* values as due to a combination of medium heterogeneity and extended near-field sources. The azimuths rotate parallel to the extensional trend (NW-SE) in the eastern caldera independently of the starting source polarization (Extended Data Fig. 7b); yet only near-field coastline sources reproduce azimuths perpendicular to the primary direction of the transfer structure. However, the lowest residuals are produced by the heterogeneous case with far line sources (residuals of 202 against 295).

Changes of horizontal noise polarization with swarms - 2012

High frequency (1-5 Hz) horizontal noise loses polarization (*R*) permanently near the location of the last eruption of the volcano (Monte Nuovo, 1538 AD)[8] after the strongest swarm recorded at the caldera between 1984 and 2019 (Extended Data Fig. 8, right). An unequal variance t-test confirmed ($p<0.05$) the hypothesis that the two sample populations (before and after September 2012) have different means. The permanent decrease of *R* is the likely consequence of fluids that permeated the area, saturating and isotropizing the system[22]. Between 0.2 Hz and 1 Hz (left) the hypothesis of the unequal mean is confirmed only considering data between June 2012 and January 2013. The cause is a small swarm in April 2012 that decreases *R* temporarily. After this swarm we observe a progressive low-frequency increase, indicative of pressurization of the deeper systems.

Declarations

Author contributions

S.P. conceived the initial idea to use the resultant length of polarization vector as a tool to image the medium properties, analysed all seismic data and performed all the measurements of seismic polarization from ambient noise through years, months, and daily analyses. L. D. S. performed the wave-equation modelling, created the tools for the generation of Figures to interpret polarization with existing geophysical models, and wrote the first draft of the paper. The authors completed the manuscript together.

Competing interests

The authors declare no competing financial interests.

Materials & Correspondence

Data files representing the polarization results and codes used to create the figures in the main text and to perform wave-equation modelling are available at the Open Science Framework, link osf.io/kqtbp. Correspondence, request for raw noise data and data-analysis software can be sent to L. D. S.

Acknowledgments

We thank the staff at the INGV-Sezione di Napoli, Osservatorio Vesuviano, for providing compiled seismic catalogues, the routine locations of volcano tectonic earthquakes, and the access to real-time data. Giuseppe Vilardo and Agata Siniscalchi provided the shape files used to plot faults and fractures and the resistivity model. The interpretation is supported by the Terrestrial Magmatic Systems (TeMaS) project, granted by the Rheinland-Pfalz Land and the Universities of Mainz, Frankfurt and Heidelberg (Germany).

References

1. Pischiutta, M., Salvini, F., Fletcher, J., Rovelli, A., & Ben-Zion, Y. Horizontal polarization of ground motion in the Hayward fault zone at Fremont, California: dominant fault-high-angle polarization and fault-induced cracks. *Geophysical Journal International*, **188**(3), 1255-1272 (2012).
2. Pischiutta, M., M. Fondriest, M. Demurtas, F. Magnoni, G. Di Toro, and A. Structural control on the directional amplification of seismic noise (Campo Imperatore, central Italy). *Earth and Planetary Science Letters* **471**: 10-18 (2017).
3. Sparks, R. S. J., Biggs, J., & Neuberg, J. W. (2012). Monitoring volcanoes. *Science*, **335**(6074), 1310-1311.
4. Carlino, S., Kilburn, C. R., Tramelli, A., Troise, C., Somma, R., & De Natale, G. Tectonic stress and renewed uplift at Campi Flegrei caldera, southern Italy: new insights from caldera drilling. *Earth and planetary science letters*, *420*, 23-29 (2015).
5. Kilburn, C. R., De Natale, G., & Carlino, S. Progressive approach to eruption at Campi Flegrei caldera in southern Italy. *Nature Communications*, **8**(1), 1-8 (2017).
6. Chiodini, G., Paonita, A., Aiuppa, A., Costa, A., Caliro, S., De Martino, P., ... & Vandemeulebrouck, J. Magmas near the critical degassing pressure drive volcanic unrest towards a critical state. *Nature Communications*, **7**(1), 1-9 (2016).
7. Giudicepietro, F., Chiodini, G., Avino, R., Brandi, G., Caliro, S., De Cesare, W., ... & Macedonio, G. Tracking Episodes of Seismicity and Gas Transport in Campi Flegrei Caldera Through Seismic, Geophysical, and Geochemical Measurements. *Seismological Society of America*, **92**(2A), 965-975 (2021).
8. Arienzo, I., Moretti, R., Civetta, L., Orsi, G., & Papale, P.. The feeding system of Agnano–Monte Spina eruption (Campi Flegrei, Italy): Dragging the past into present activity and future scenarios. *Chemical Geology*, **270**(1-4), 135-147 (2010).

9. Amoruso, A., Crescentini, L., & Sabbetta, I. Paired deformation sources of the Campi Flegrei caldera (Italy) required by recent (1980–2010) deformation history. *Journal of Geophysical Research: Solid Earth*, **119**(2), 858-879 (2014).
10. Pepe, S., De Siena, L., Barone, A., Castaldo, R., D'Auria, L., Manzo, M., Casu, F., Fedi, M., Lanari, R., Bianco, F. and Tizzani, P. Volcanic structures investigation through SAR and seismic interferometric methods: The 2011–2013 Campi Flegrei unrest episode. *Remote Sensing of Environment*, **234**, p.111440 (2019).
11. Siniscalchi, A., Tripaldi, S., Romano, G., Chiodini, G., Improta, L., Petrillo, Z., D'Auria, L., Caliro, S. and Avino, R. Reservoir structure and hydraulic properties of the Campi Flegrei geothermal system inferred by audiomagnetotelluric, geochemical, and seismicity study. *Journal of Geophysical Research: Solid Earth*, **124**(6), pp.5336-5356 (2019).
12. Ardhuin, F., Stutzmann, E., Schimmel, M., & Mangeney, A. Ocean wave sources of seismic noise. *Journal of Geophysical Research: Oceans*, **116** (C9) (2011).
13. Lecocq et al., Global quieting of high-frequency seismic noise due to COVID-19 pandemic lockdown measures. *Science*, **369**(6509), 1338-1343 (2020).
14. Brenguier, F., Shapiro, N. M., Campillo, M., Nercessian, A., & Ferrazzini, V. 3-D surface wave tomography of the Piton de la Fournaise volcano using seismic noise correlations. *Geophys. Res. Lett.*, **34**, 2305-2309 (2007).
15. Brenguier, F., M. Campillo, T. Takeda, Y. Aoki, N. M. Shapiro, X. Briand, K. Emoto, and H. Miyake. Mapping pressurized volcanic fluids from induced crustal seismic velocity drops. *Science* **345**, no. 6192: 80-82 (2014).
16. Jaxybulatov, K., Shapiro, N. M., Koulakov, I., Mordret, A., Landès, M., & Sens-Schönfelder, C. A large magmatic sill complex beneath the Toba caldera. *Science*, **346**, 617-619 (2014).
17. De Siena, L., Sammarco, C., Cornwell, D. G., La Rocca, M., Bianco, F., Zaccarelli, L., & Nakahara, H. Ambient seismic noise image of the structurally controlled heat and fluid feeder pathway at Campi Flegrei caldera. *Geoph. Res. Lett.*, **45**, 6428-6436 (2018).
18. Brenguier, F., Shapiro, N. M., Campillo, M., Ferrazzini, V., Duputel, Z., Coutant, O., & Nercessian, A. Towards forecasting volcanic eruptions using seismic noise. *Nature Geoscience*, **1**, 126-130 (2008).
19. Zaccarelli, L., & Bianco, F. (2017). Noise-based seismic monitoring of the Campi Flegrei caldera. *Geophysical Research Letters*, **44**(5), 2237-2244.
20. Nakata, N., Boué, P., Brenguier, F., Roux, P., Ferrazzini, V., & Campillo, M. Body and surface wave reconstruction from seismic noise correlations between arrays at Piton de la Fournaise volcano. *Geophys. Res. Lett.*, **43**(3), 1047-1054 (2016).
21. Yates, A. S., Savage, M. K., Jolly, A. D., Caudron, C., & Hamling, I. J. Volcanic, coseismic, and seasonal changes detected at White Island (Whakaari) Volcano, New Zealand, using seismic ambient noise. *Geophysical Research Letters,* **46**(1), 99-108 (2019).
22. Saade, M., Araragi, K., Montagner, J. P., Kaminski, E., Roux, P., Aoki, Y., & Brenguier, F. Evidence of reactivation of a hydrothermal system from seismic anisotropy changes. *Nature communications*,

10(1), 1-8 (2019).

23. Vanorio, T., & Kanitpanyacharoen, W. Rock physics of fibrous rocks akin to Roman concrete explains uplifts at Campi Flegrei Caldera. *Science*, **349**(6248), 617-621 (2015).
24. De Siena, L., Amoruso, A., Pezzo, E. D., Wakeford, Z., Castellano, M., & Crescentini, L. Space-weighted seismic attenuation mapping of the aseismic source of Campi Flegrei 1983–1984 unrest. *Geoph. Res. Lett.*, **44**, 1740-1748 (2017a).
25. De Siena, L., Chiodini, G., Vilardo, G., Del Pezzo, E., Castellano, M., Colombelli, S., Tisato, N. & Ventura, G. Source and dynamics of a volcanic caldera unrest: Campi Flegrei, 1983–84. *Scientific reports*, **7**, 1-13 (2017b).
26. Calò, M., & Tramelli, A. Anatomy of the Campi Clegrei caldera using enhanced seismic tomography models. *Scientific reports*, **8**(1), 1-12 (2018).
27. Petrosino, S., Cusano, P., & Madonia, P. Tidal and hydrological periodicities of seismicity reveal new risk scenarios at Campi Flegrei caldera. *Scientific reports*, **8**(1), 1-12 (2018).
28. Ricco, C., Petrosino, S., Aquino, I., Del Gaudio, C., & Falanga, M. Some investigations on a possible relationship between ground deformation and seismic activity at Campi Flegrei and Ischia volcanic areas (Southern Italy). *Geosciences*, **9**(5), 222 (2019).
29. Cusano, P., Petrosino, S., De Lauro, E., & Falanga, M. The whisper of the hydrothermal seismic noise at Ischia Island. *Journal of Volcanology and Geothermal Research*, **389**, 106693 (2020).
30. De Lauro, E., De Martino, S., Falanga, M., & Petrosino, S. Synchronization between tides and sustained oscillations of the hydrothermal system of Campi Flegrei (Italy). Geochemistry, Geophysics, Geosystems, **14**(8), 2628-2637 (2013)
31. Bellucci Sessa, E., Castellano, M., & Ricciolino, P. (2021). GIS applications in volcano monitoring: the study of seismic swarms at the Campi Flegrei volcanic complex, Italy. *Advances in Geosciences*, **52**, 131-144 (2021).
32. Chiodini, G., Caliro, S., Avino, R., Bini, G., Giudicepietro, F., De Cesare, W., ... & Tripaldi, S.. Hydrothermal pressure-temperature control on CO2 emissions and seismicity at Campi Flegrei (Italy). *Journal of Volcanology and Geothermal Research*, **414**, 107245 (2021).
33. Young, N., Isaia, R., & Gottsmann, J. Gravimetric Constraints on the Hydrothermal System of the Campi Flegrei Caldera. *Journal of Geophysical Research: Solid Earth*, **125**(7), e2019JB019231 (2020).
34. Acocella, V., Salvini, F., Funiciello, R., & Faccenna, C. The role of transfer structures on volcanic activity at Campi Flegrei (Southern Italy). *Journal of Volcanology and Geothermal Research*, **91**(2-4), 123-139 (1999).
35. Vilardo, G., Isaia, R., Ventura, G., De Martino, P. & Terranova, C. InSAR Permanent Scatterer analysis reveals fault re-activation during inflation and deflation episodes at Campi Flegrei caldera. *Remote Sensing of Environment* **114**, 2373–2383 (2010).
36. Isaia, R., Vitale, S., Di Giuseppe, M. G., Iannuzzi, E., Tramparulo, F. D. A., & Troiano, A. Stratigraphy, structure, and volcano-tectonic evolution of Solfatara maar-diatreme (Campi Flegrei, Italy). *GSA*

Bulletin, **127**(9-10), 1485-1504 (2015).

37. Vitale, S. & Isaia, R. Fractures and faults in volcanic rocks (Campi Flegrei, Southern Italy): Insight into volcano-tectonic processes. *International Journal of Earth Sciences* **103**, 801–819 (2014).
38. Di Luccio, F., Pino, N. A., Piscini, A., & Ventura, G. Significance of the 1982–2014 Campi Flegrei seismicity: Preexisting structures, hydrothermal processes, and hazard assessment. *Geophysical Research Letters*, **42**(18), 7498-7506 (2015).
39. Bianco, F., & Zaccarelli, L. A reappraisal of shear wave splitting parameters from Italian active volcanic areas through a semiautomatic algorithm. *Journal of seismology*, **13**(2), 253-266 (2009).
40. Long, M. D., & Becker, T. W. Mantle dynamics and seismic anisotropy. *Earth and Planetary Science Letters*, **297**(3-4), 341-354 (2010).
41. Faccenda, M., Burlini, L., Gerya, T. V., & Mainprice, D. Fault-induced seismic anisotropy by hydration in subducting oceanic plates. *Nature*, **455**(7216), 1097-1100 (2008).
42. Hillers, G., & Campillo, M. (2016). Fault zone reverberations from cross-correlations of earthquake waveforms and seismic noise. *Geophysical Journal International*, **204**(3), 1503-1517.
43. Petrosino, S., Ricco, C., De Lauro, E., Aquino, I., & Falanga, M. Time evolution of medium and long-period ground tilting at Campi Flegrei caldera. *Advances in Geosciences*, **52**, 9-17 (2020).
44. De Lauro, E., Petrosino, S., Ricco, C., Aquino, I., & Falanga, M. Medium and long period ground oscillatory pattern inferred by borehole tiltmetric data: New perspectives for the Campi Flegrei caldera crustal dynamics. *Earth and Planetary Science Letters*, **504**, 21-29 (2018).
45. Takagi, R., Nishida, K., Maeda, T., & Obara, K. (2018). Ambient seismic noise wavefield in Japan characterized by polarization analysis of Hi-net records. *Geophysical Journal International*, **215**(3), 1682-1699.
46. Petrillo, Z., D'Auria, L., Mangiacapra, A., Chiodini, G., Caliro, S., & Scippacercola, S. (2019). A perturbative approach for modeling short-term fluid-driven ground deformation episodes on volcanoes: A case study in the Campi Flegrei caldera (Italy). *Journal of Geophysical Research: Solid Earth*, **124**(1), 1036-1056 (2019).
47. Akande, W. G., Gan, Q., Cornwell, D. G., & De Siena, L. (2021). Thermo-Hydro-Mechanical Model and Caprock Deformation Explain the Onset of an Ongoing Seismo-Volcanic Unrest. *Journal of Geophysical Research: Solid Earth*, **126**(3), e2020JB020449.
48. Selva, J., Orsi, G., Di Vito, M. A., Marzocchi, W., & Sandri, L. (2012). Probability hazard map for future vent opening at the Campi Flegrei caldera, Italy. *Bulletin of volcanology*, **74**(2), 497-510.
49. Bevilacqua, A., Isaia, R., Neri, A., Vitale, S., Aspinall, W. P., Bisson, M., ... & Rosi, M. Quantifying volcanic hazard at Campi Flegrei caldera (Italy) with uncertainty assessment: 1. Vent opening maps. *Journal of Geophysical Research: Solid Earth*, **120**(4), 2309-2329 (2015).
50. Carcione, J. M.. *Wave Fields in Real Media: Wave Propagation in Anisotropic, Anelastic, Porous and Electromagnetic Media*. Elsevier, Amsterdam, The Netherlands (2014).

Figures

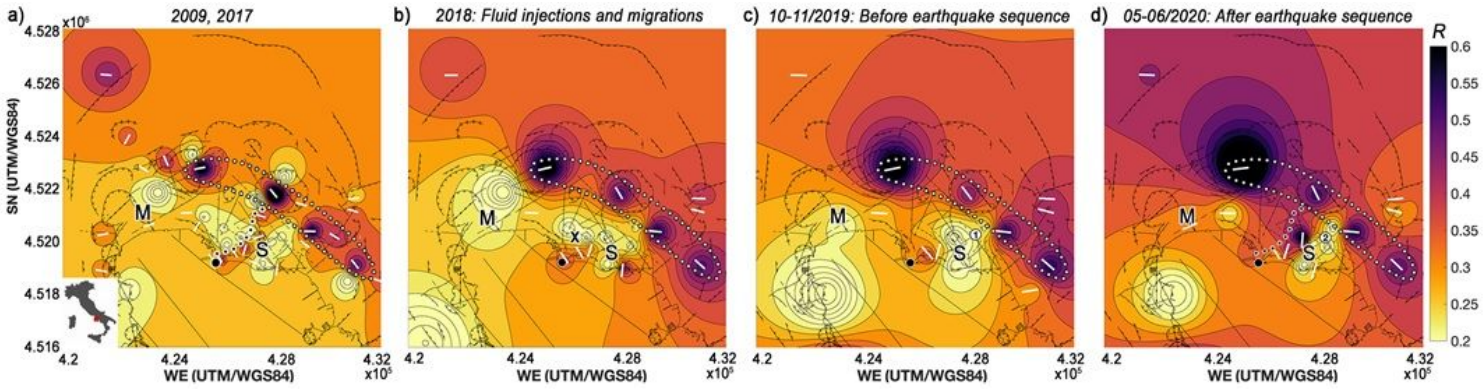

Figure 1

Maps of resultant length and azimuths from ambient noise at Campi Flegrei. a) The resultant length (R) is plotted with a squared interpolation from each station between 0.2 and 1 Hz during periods of low seismic release (2009, 2017). The white continuous segments show the corresponding azimuths (only for R>0.25). The patterns are imposed over fault strikes, fractures and craters35-37. The Solfatara crater (S) and Monte Nuovo (M) are marked on the maps. The wide black dot is the stationary point of maximum vertical deformation for the last 36 years9-10. The dotted black line marks the part of the transfer structure with R>0.31. The dotted white line contours the portion of the NW-SE extensional faults that show R>0.5 and the same azimuths over the decade. b-d) Same maps obtained using noise recorded over six months in 2018 (b, the black cross shows the centre of the high-attenuation anomaly in Fig. 2a), two months before the Md3.1 (c, December 6th, 2019, circled number 131) and two months after the Md3.3 (d, April 26th, 2020, circled number 231, here the transfer structure reappears).

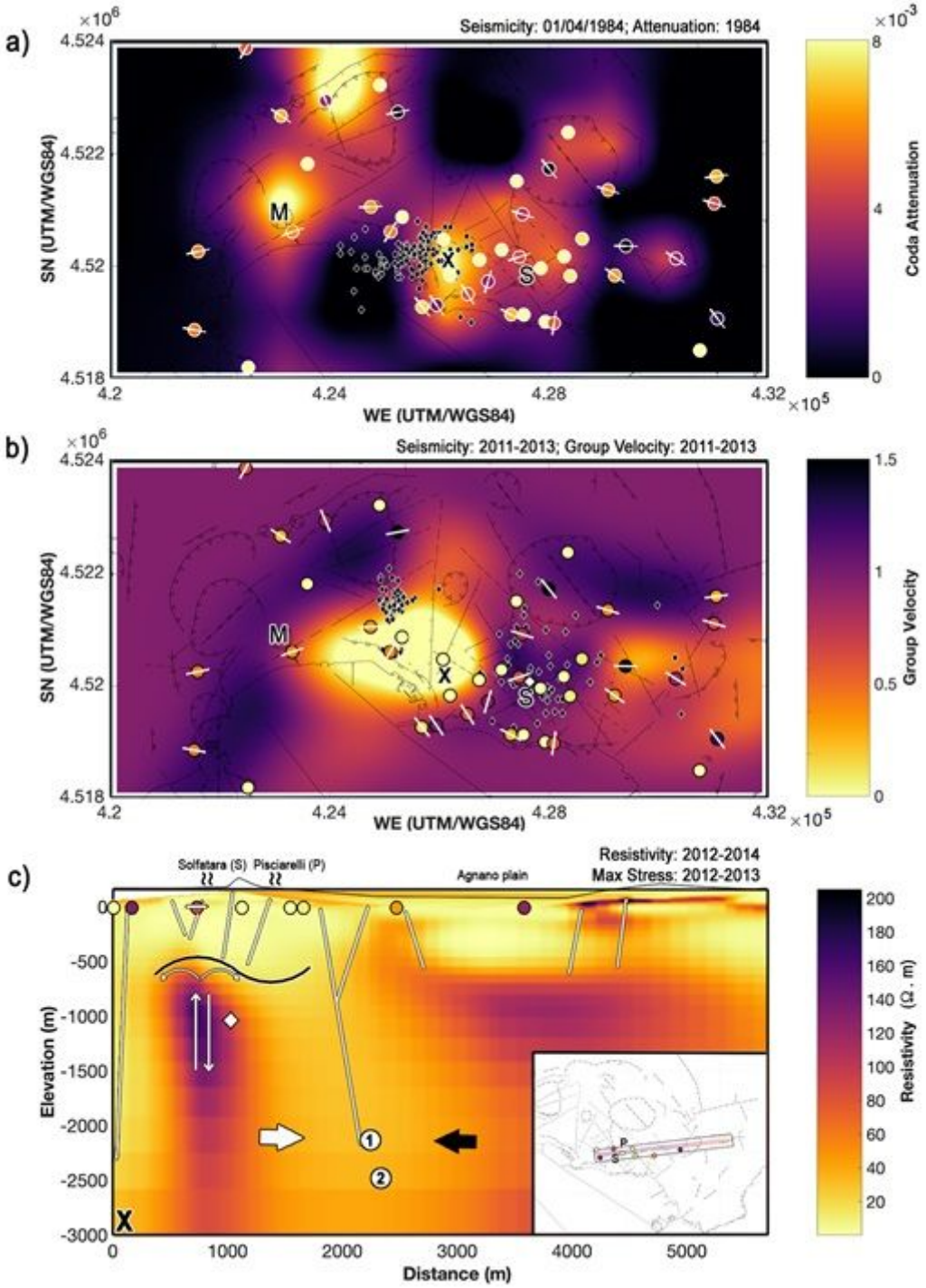

Figure 2

Comparison of polarization with velocity, attenuation, resistivity and stress. a) The low-frequency resultant lengths (colour-mapped in Fig. 1) and azimuths obtained at stations recording in 2009 and 2017 are compared with the high-attenuation signature (black cross, coda attenuation of 0.00826) of the injections6,25 that opened the low-velocity hydrothermal system in 198425. The black diamonds show the earthquakes recorded on April 1st (maximum Md=4.1)25. b) In 2011-2013, a low-velocity17 aseismic,38 reservoir was expanding from the injection location4,5,10,17. The white diamond at

Solfatara is the point of highest lateral stress in 2011-201310. The black diamonds show seismicity in the same period. c) A resistive plume feeds fumaroles at Solfatara and Pisciarelli (thin white arrows). Faults (white lines) and a clay cap (continuous black curve)11 constrain the plume. The profile and nearby seismic stations are shown inside the rectangle in the lower inset. The white thick arrow marks the east-directed expansion4,10 from the deep injection point. The black thick arrow shows the west-directed extension of the caldera-bounding faults35-37 that bind a resistive metasomatic reservoir11 under the Agnano plain. The Md3.1 (circled number 1) and Md3.3 (circled number 2) earthquakes31 nucleate on a deep fault within conductive liquid-bearing metasediments11.

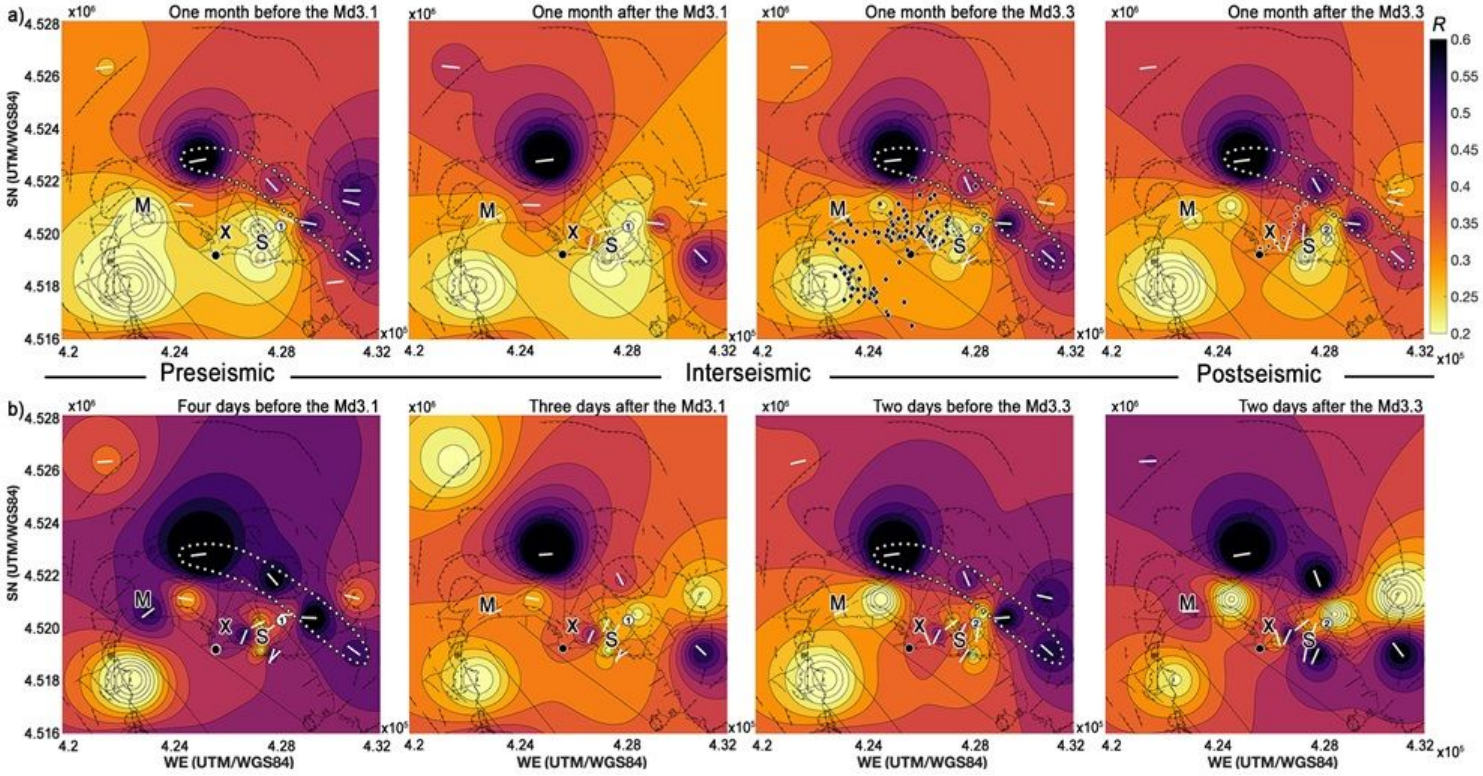

Figure 3

Build-up and release of fluid-induced stress: a) The polarization parameters have been plotted using data spread across one month before and after both the Md3.1 and the Md3.3 earthquakes. Black diamonds correspond to the earthquake locations between June and December 198425. The white dotted line contours the extensional structure when visible and continuous. b) Polarization parameters computed using three hours of noise on a single day, before and after the Md3.1 and Md3.3. Differences in temporal patterns take into account modelled injection-induced fluid flow and deformation47.

Supplementary Files

This is a list of supplementary files associated with this preprint. Click to download.

- ExtendedData.pdf